ISSN: 2639-0108

Research Article

Advances in Theoretical & Computational Physics

Classical molecular dynamics study of structural properties of pristine and defective mono-layer 2D h-BNNSs

Magopa T.M Kekana[1], Thuto E. Mosuang[1]*, Nikiwe Mhlanga[2], Mokete A. Mahladisa[1], Lucky M. Sikhwivhilu[2,3]*

[1]Department of Physics, University of Limpopo, Private Bag x1106, Sovenga, 0727, Limpopo Province, South Africa

[2]DSI/Mintek Nanotechnology Innovation Centre, Randburg, 2194, South Africa

[3]Department of Chemistry, Faculty of Science, Engineering and Agriculture, University of Venda, Private Bag X5050, Thohoyandou 0950, South Africa

***Corresponding author:**
Lucky Sikhwivhilu, DSI/Mintek Nanotechnology Innovation Centre, Advanced Materials Division, Mintek, Randburg, 2125, South Africa.

Submitted: 02 Nov 2022; **Accepted:** 07 Nov 2022; **Published:** 15 Nov 2022

Citation: *T.M Kekana, M., E Mosuang, T., Mhlanga, N., Mahladisa, M. A., Sikhwivhilu, L. M. (2022). Classical molecular dynamics study of structural properties of pristine and defective mono-layer 2D h-BNNSs. Adv Theo Comp Phy, 5(4), 616-628.*

Abstract

The structural, stability and vacancy properties of both defect-free and defected 2D h-BNNSs were studied using the classical molecular dynamics (MD) approach. The calculations were performed in the canonical (NVT Evans) and isothermal-isobaric (NPT Hoover) ensembles using the Tersoff potentials with the Verlet leapfrog algorithm to obtain reliable structural properties and energies for defect-free, boron (B) and nitrogen (N) vacancies. B and N defect energies were calculated relative to the bulk defect-free total energies, and the results suggest that N vacancy is the most stable vacancy as compared to the B vacancy. The radial distribution functions (RDF) and structure factors were used to predict the most probable structural form. Mean square displacement (MSD) suggests that the mobility of B and N atoms in the system increases with an increase in the surface area of the nanosheets. Results obtained were compared with the bulk defect-free h-BNNSs.

Keywords: *Molecular Dynamics, Defect-Free Energies, Defects Energies, Radial Distribution Functions, Structure Factors, Mean Square Displacement, 2D h-BNNSs.*

Table 1: Nomenclature description of all abbreviations with their units.

Abbreviations	Description	Abbreviations	Description
MD	Molecular dynamics	h-BNNS576	Supercell with 576 atoms
DFT	Density functional theory	**ΔS**	Change in entropy
2D h-BNNSs	Two dimensional hexagonal boron nitride nanosheets	E_{vac}	Vacancy energy
BNNTs	Boron nitride nanotubes	E_{defect}	Defected total energy
NVT	Canonical ensemble	$E_{(defect\ free)}$	Defect free total energy
NVE	Micro canonical ensemble	V_N / ***N-vac***	Nitrogen vacancy
NPT	Isothermal-isobaric ensemble	V_B / ***B-vac***	Boron vacancy
FET's	Field effects transistors	**T**	temperature
N_2O	Nitrous Oxide	**K**	Kelvins
RDF's/$(g_{AB}(r))$	Radials distribution functions	**eV**	Electron volts
SF/(S(k))	Structure factors	**Å**	Angstroms
MSD	Mean square displacement	**ps**	Picoseconds
h-BNNS144	Supercell with 144 atoms	**°C**	Degree Celsius
h-BNNS324	Supercell with 324 atoms		

Introduction

Classical molecular dynamics (MD) simulations play an important role in the modelling of materials properties and processes for a better understanding of their applications. The approach is applicable and transferable across the fields of physics, chemistry, material science, nanotechnology and engineering [1]. Additionally, the study of mechanical, optical, elastic and electrical properties of materials is important for different industrial applications. Certain studies have suggested that two dimensional (2D) hexagonal boron nitride (h-BN) and its derivatives have better mechanical properties over the layered pristine graphene [2]. Such outstanding properties are essential in the production of nano devices applied in sensing and electronics. Naturally, h-BN is thermally stable and chemically inert in air up to 1500 °C [3]. Different researchers using various approaches have successfully investigated the mechanical robustness of h-BN. Srivastava *et al.* [4] have effectively used the *ab anitio* density functional theory (DFT) to study the structural defects in h-BNC_2 sheets. The DFT approach is more appropriate for calculations at the electronic level as it can only accumulates a few hundreds of atoms due to non-trivial nature of calculations involved and memory effects. On the other hand, the classical MD is efficient on simulating large systems of ~10 million atoms on time length of 1 ns [5]. Mermin [6] and later Kresse et al. [7] studies demonstrate the feasibility of classical MD methods in the conclusive investigations on h-BN nanosheets (h-BNNSs). Such studies suggest that the 2D materials transition is still of first order as observed in the ordinary 3D materials. The fact is that, the quality of the acquired classical MD results relies on the accuracy of the chosen potential model [8]. The latter depend strongly on the applications of the material.

In this article, the material of interest is the monolayer h-BN. The mono-layer h-BN has potential to be the most stable and attractive crystalline 2D material at room temperature. In recent reports, h-BN nanosheets have been demonstrated to possess dielectric character in electronics which could also function as a carrier catalyst [9-12] in the fabrication of graphene based field effect transistors (FETs) [13, 14]. h-BN nanosheets can also act as tunnelling barriers between graphene layers [15]. These h-BNNSs have been used to protect metal surfaces at elevated temperatures. However, the compelling synthesis method has not been properly described. In certain industries, h-BN nanosheets have been employed as fire resistant coating for wood, which does not carbonize up to 900 °C [16]. When compared to boron nitride nanotubes (BNNTs) and graphene; BNNTs are now readily theoretically predicted and experimentally synthesised. In this form, BNNTs were found to be the potential gas detectors and an efficient catalyst for the nitrous oxide (N_2O) reduction reaction [17] due to their great chemical properties and high thermal stability. It would be of great industrial benefit to also acquire the BN nanosheets with these outstanding properties. Graphene also became one of the most popular material for various technological applications including sensors [18, 19] surface coating against corrosion etc. Such applications were inspired by the graphene's perfect flat structure and ultrahigh fracture strength [20] and fatigue life [21] owing to being chemically inert and impermeable to gases and some liquids [22]. To quantify 2D materials scope, probing similar applications on the h-BNNSs will sustain the layered materials functions.

In this article, the proposed potential model is that by Tersoff [23, 24] from his original papers which is normally referred to as the Tersoff potential. There are many different parameterisations of this Tersoff potential available in the literature, mostly for elements of group IV [23 - 27] and groups III-V [28-33]. In this case, the set of parameters were extracted from Matsunaga *et al.* [8] paper to describe the interactions between boron (B) and nitrogen (N) atoms within the BN system. Furthermore, these parameters have been used successfully to study the thermal transport and mechanical properties of more complex materials such as hybrid graphene-boron nitride, graphitic carbon nitrides and boron-carbonitrides [34, 35]. Moreover, the highlight will be on the stability of vacancy defects on the mono-layer h-BN or just 2D h-BNNSs. Specifically, the manuscript reports on the modelling of the structural and thermal properties of h-BNNSs and how native vacancy defects in mono-layer h-BN get created.

2. Methodology

2.1 DL_POLY computational process

Molecular dynamics (MD) is a computational method used to study the motion of atoms and molecules in a system. In setting and running a MD simulation, the first task is to decide which energy model to use to describe the interactions within the system. Then the initial configuration has to be chosen in such a way that it favors the potential model used. In this report, all classical MD simulations have been performed using the DL_POLY [28] computer code. Tersoff potentials [24] with parameters of Matsunaga *et al.* [8] have been used to accurately reproduce the interactions between B and N atoms of mono-layered BN system. The calculations are based on the canonical (NVT Evans) and isothermal-isobaric (NPT Hoover) ensembles.

The canonical and isothermal-isobaric ensembles were preferred over micro-canonical (NVE) ensemble [36]. Simulations performed at constant temperature and constant pressure mimic real life situations, and both the NVT and NPT ensembles comply with the objectives. Additionally, simulations in the NVT ensemble maintains the number of particles, volume and temperature constant, which are distinguished by mainly two approaches: coupling the system to a heat bath and rescaling the velocities accordingly or make use of the extended phase approach.

Simulations in the NPT ensemble are performed such that the volume of the system is adjusted in a way that the average internal pressure is the same as the applied external pressure Slotman *et al.* [37]. A model consisting of three supercells of 144 atoms (72 B and 72 N atoms), 324 atoms (162 B and 162 N atoms) and 576 atoms (288 B and 288 N atoms) each were set up. All the supercells were relaxed well with suitable hexagonal configurations and preferred Tersoff potential parameters. The 2D hexagonal configurations in the supercells was made possible by creating a vacuum between the adjacent layers of the bulk h-BN. This was achieved by stretching the ordinary interlayer spacing from the experimental 6.656 to 7.900 Å in all the three systems [38, 48, 49]. The MD simulations were allowed to run with a 0.001 ps timestep, for a period of 5000 steps and an equilibration after every 500 steps. For data analysis from the output files,

the radial distribution functions (RDF) and structure factors (SF) were plotted to understand the structural configurations whilst the mean square displacements (MSD) were plotted to determine the diffusion constants. The same procedure was repeated on the B and N vacancies on the systems for good comparison.

3. Results and Discussion

3.1. Structural properties of h-BNNSs

3.1.1. Radial Distribution Functions and Structure Factors

The RDF or pair correlation function is a powerful tool to analyse the structural information of a material. It is estimated by considering the average distance between all pairs of atoms in a given material. In general, if $g_{AB}(r)$ is the radial distribution function, then $g_{AB}(r)r$ is proportional to the probability of finding an atom of type B at a distance between r and $r + \Delta r$ from an atom of type A [39] where B and A represents B and N atoms. On a two-dimensional system, the equation would be:

$$g_{AB}(r) = \frac{\Delta n_{AB}}{2\pi r \Delta r \rho_B} \qquad (1)$$

where ρ_B is the average density of species B in the entire material and Δn_{AB} is the average number of particles of type B present in the angular region between r and $r + \Delta r$ with an A atom at the centre (equation 1). The averaging is over all the A atoms present in the simulation volume. The radial distribution functions must be delta functions at 0 K, as there are unique values for the radii of the various neighbouring shells. However, due to thermal vibrations, these distances become blurred as the temperature of the system increases. The delta functions broaden into smooth peaks. The peak width increases with temperature. The width is in fact proportional to the root mean squared displacement of the atoms from their equilibrium position.

The position of the n^{th} peak in $g_{AB}(r)$ would correspond to the mean distance of the B atom from the A atom in n^{th} neighbour positions. Thus, the value of $g_{AB}(r)$ at any r decreases as the temperature increases due to thermal broadening [39, 40]. Structural properties of mono-layer 2D h-BNNS have been precisely analysed using the radial distribution functions ($g_{AB}(r)$) and structure factors *(S(k))*. The observed sharp peaks, separations and heights in Figure 1, are all the characteristics of a lattice structure exhibited by a solid material. In the $g_{AB}(r)$ of nanosheet, the peak positions (abscissa values) correspond to the first, second, and further nearest neighbor distances between the atoms of the hexagonal atomic system on the plane sheet.

Table 2 depicts the peak positions of first and second neighbor distances of h-BNNS144, h-BNNS324 and h-BNNS576 at equilibrium temperature of 300 K. The peak positions of h-BNNS144 atomic positions for the B-B, first and second nearest neighbor distances appear at 2.47 and 2.69 Å respectively. In the same manner, B-N first and second nearest neighbor distances appear at 1.41 and 2.81 Å respectively. Likewise the N-N, first and second nearest neighbor distances appear at 2.47 and 2.69 Å. In a similar manner, Table 2 provides the same information for h-BNNS324 and h-BNNS576 supercells respectively. The B-N bond lengths of pristine mono-layer h-BN nanosheets were respectively found to be 1.41 Å, 1.44 Å and 1.44 Å for 144, 324 and 576 h-BNNSs supercells. Obtained results concur with various studies on h-BN nanosheets as reported by Thomas *et al.* [39] and many bulk h-BN studies [41, 42]. A typical visualisations of the 2D h-BN mono-layer nanosheet at 300 K for all the supercells is shown in Figure 2. Here the hexagonal honeycomb with alternating B and N atoms [43 - 47] is evident in Figure 2(a, b and c). Further on Figure 2(d, e and f) present the same visuals perpendicular to the nanosheet planes. The results demonstrate that the possibility of more realistic interpretation of the 2D systems as the sampling of the planar sheets is enhanced with the number of atoms or larger planar nanosheets.

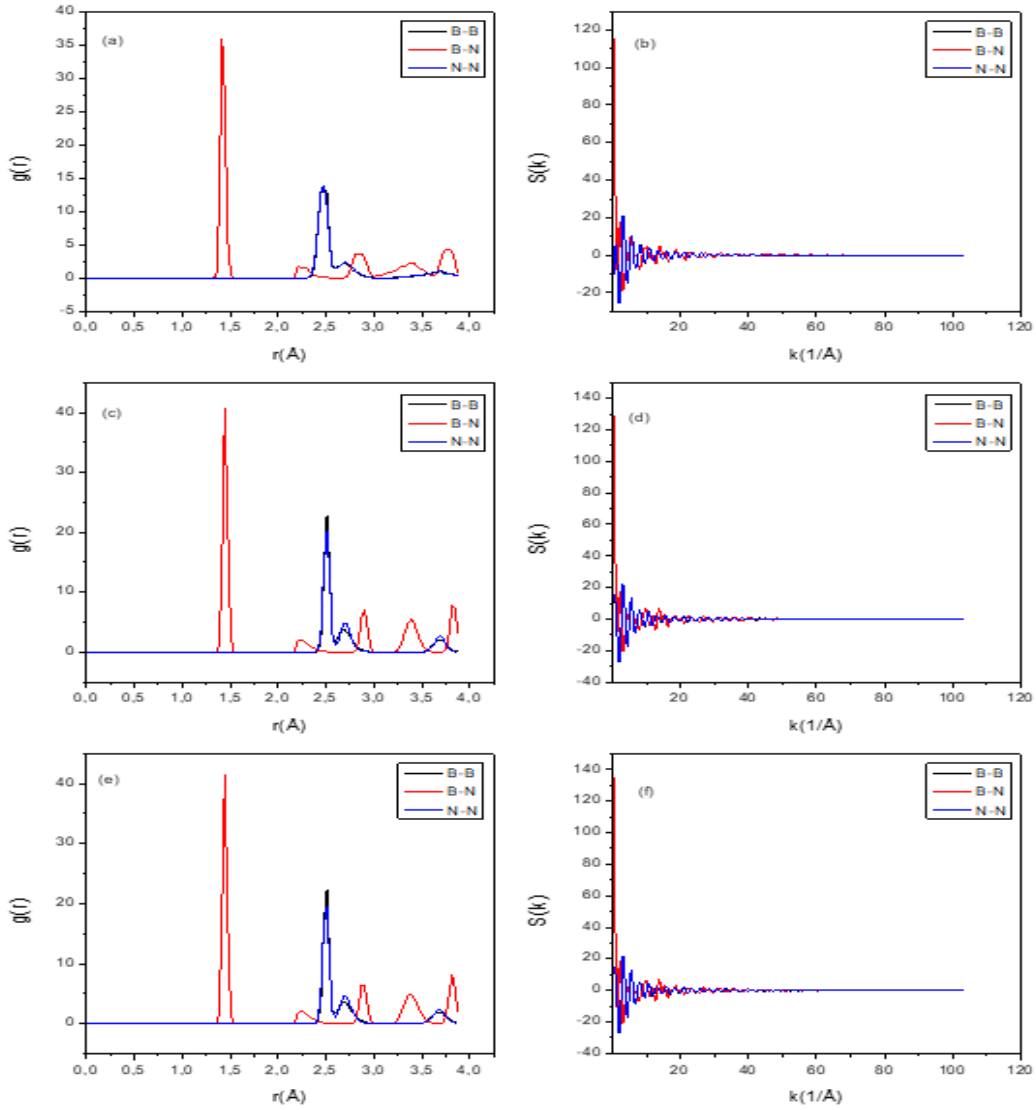

Figure 1: Radial Distribution Functions together with their corresponding structure factors for (a) and (b) h-BNNS144 supercell, (c) and (d) h-BNNS324 supercell and (e) and (f) h-BNNS576 supercell.

Table 2: First and second nearest neighbouring distances (r_1 and r_2) and corresponding number of atoms (n_1 and n_2) in h-BNNS144, h-BNNS324 and h-BNNS576 supercells at 300 K.

Supercells	Atomic bonds	r_1(Å)	n_1	r_2(Å)	n_2
h-BNNS144	B-B	2.47	0.82	2.69	0.24
	B-N	1.41	1.64	2.81	0.27
	N-N	2.47	0.82	2.69	0.22
h-BNNS324	B-B	2.51	1.73	2.69	0.34
	B-N	1.44	1.86	2.90	0.43
	N-N	2.51	1.55	2.69	0.45
h-BNNS576	B-B	2.51	2.45	2.66	0.64
	B-N	1.44	1.86	2.90	0.76
	N-N	2.51	2.15	2.72	0.50

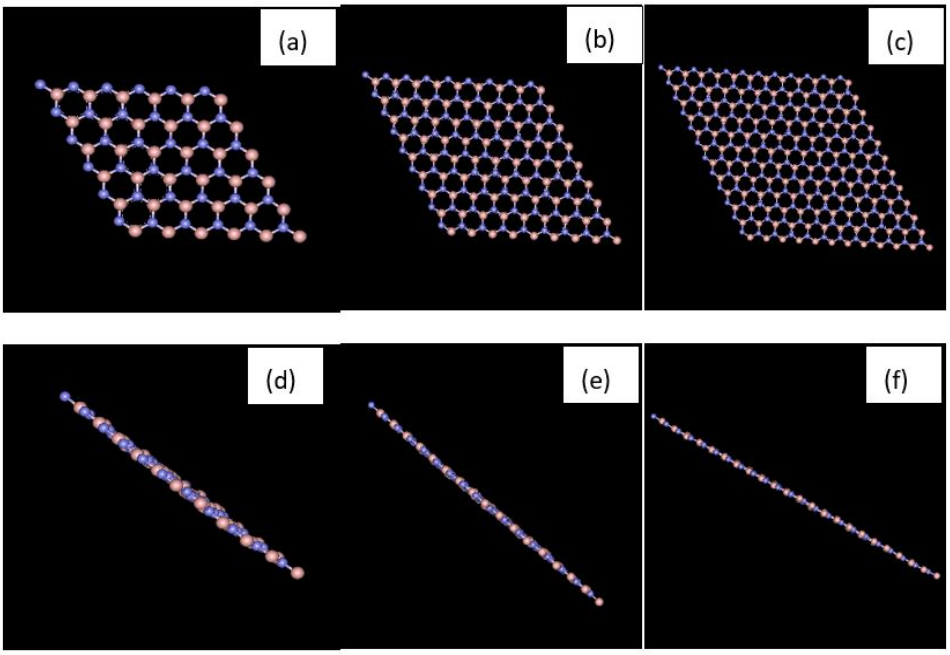

Figure 2: The visualisation of the optimised structure (a), (b) and (c) represented by alternating B (brown spheres) and N (blue spheres) atoms together with its alignment perpendicular to the plane (d), (e) and (f) of defect-free nanosheets for h-BNNS144, h-BNNS324 and h-BNNS576 supercells at 300 K.

Furthermore, the lattice parameters of h-BNNSs were calculated at equilibrium for all the supercells, which were found to be in good agreement with what has been reported previously on the material [38, 48, 49]. The Tersoff potential used in the present study reliably gives the lattice parameters of all the three supercells closer to the experimental values. The experimental lattice parameters of bulk h-BN at room temperature were reported to be a = 2.504 and c = 6.625 Å with an average B-N bond length of 1.44 Å [38]. MD simulations using a modified Albe, Moller and Heining interatomic potential gives the equilibrium lattice parameter of a = 2.532 and c = 6.656 Å at 0 K with an average B-N bond length of 1.46 Å [48, 49]. In this work, at room temperature using the Tersoff potentials, the lattice parameters of the supercells (144, 324 and 576 atoms) were respectively found to be a = 2.477 Å, 2.507 Å and 2.507 Å with an averaging B-N bond length of 1.41 Å, 1.44 Å and 1.44 Å. The obtained MD lattice parameters of the materials, found to be closer to the experimental reported results, which brings us closer to the real life situation. Such an observation makes MD method a reliable candidate for modelling of materials.

Table 3: Supercell and unit cell lattice parameters at minimum together with the corresponding minimum energy.

Supercells	h-BNNS144	h-BNNS324	h-BNNS576
Supercell lattice parameter (a_0) (Å)	14.563	22.568	29.897
Unit cell lattice parameter (a_0) (Å)	a = b = 2.477	a = b = 2.507	a = b = 2.507
Literature unit cell lattice parameter (a_0) (Å) [38]	a = b = 2.504		
Minimum Energy (E_m) (eV)	-2.1886×10^3	-4.9155×10^3	-8.7414×10^3

These results compare fairly well with experimental values [38, 48, 49]. The lattice parameters of all the supercells were determined at minimum temperature, together with their corresponding energies. Table 3 shows a summary of lattice parameters that were found to be stabilising at a = b = 2.507 Å with an increase in the surface area (number of atoms in a plane), and their corresponding minimum energies are decreasing. In this scenario, the relationship between energy and the lattice parameter is interesting and complemented well by other calculated results [38].

3.1.2 Diffusion constants on the h-BNNSs

To explain the mobility of B and N atoms in the h-BN system, the MSD graphs were plotted in Figure 3 for h-BNNS144, h-BNNS324 and h-BNNS576 supercells and are utilised to calculate the diffusion coefficients of both B and N atoms. The diffusion coefficients are calculated as the surface area of the sheets increases. The mobility of the atoms within the surface of the material was studied for possible understanding of the planar sheet bending of the h-BN nanosheets. The results depicted in Table 4 shows the diffusion coefficients of B and N atoms respectively for h-BNNS144, h-BNNS324 and h-BNNS576 supercells at 300 K.

The value of the diffusion coefficient of the B atoms within the nanosheets increase with increasing surface area. The behaviour on the N atoms diffusion coefficients is not conclusive, as such more studies in this regard needs to be considered. These may suggest the absence of the inter-layer interactions in mono-layer h-BN may lead to an increased planar strength on the nanosheets which might also be enhanced by the ionic nature of B-N bonds. Such property does not exist in bulk h-BN due to weak inter-layer interactions. The stiffness of the nanosheets is reduced as the surface area of the nanosheets increases, which agrees with what was reported by Alem *et al.* [49].

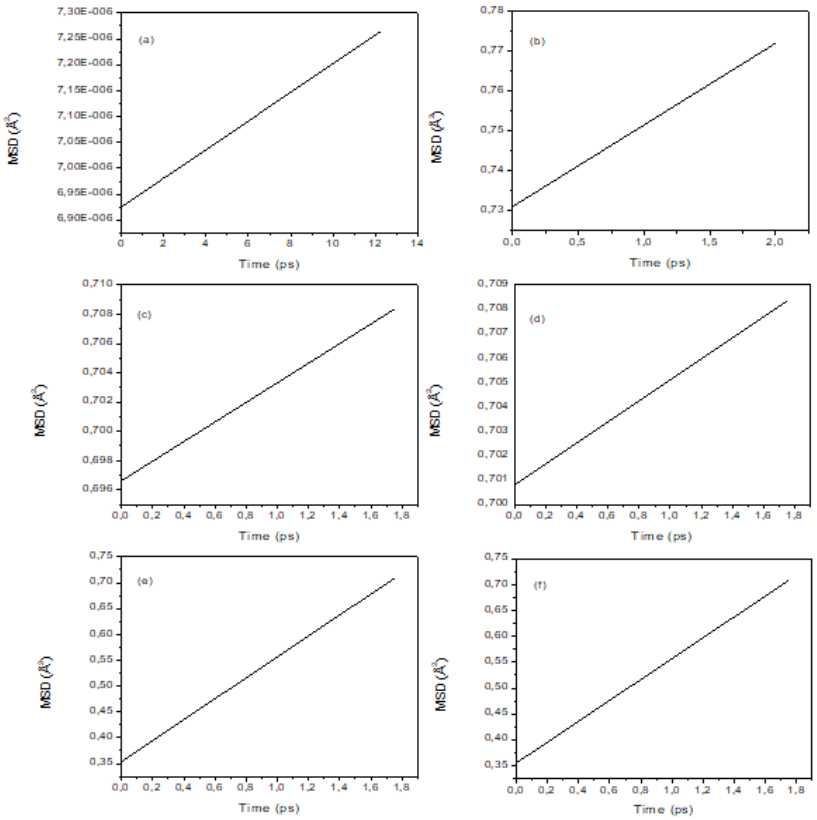

Figure 3: Mean square displacement graphs of (a) B atoms in h-BNNS144, (b) N atoms in h-BNNS144, (c) B atoms in h-BNNS324, (d) N atoms in h-BNNS324, (e) B atoms in h-BNNS576 and (f) N atoms in h-BNNS576 supercells at 300 K.

Table 4: Diffusion coefficients for both B and N atoms for all the supercells.

Supercells	Diffusion coefficient of B (Å²/ps)	Diffusion coefficient of N (Å²/ps)
h-BNNS144	2.86×10^{-8}	2.05×10^{-2}
h-BNNS324	6.68×10^{-3}	4.31×10^{-3}
h-BNNS576	2.02×10^{-1}	2.02×10^{-1}

3.2 Thermal properties of h-BNNSs

The effects of temperature on the mechanical properties of 2D h-BNNS were also examined. It is undisputable that temperature plays an important role on the mechanical properties of nanomaterials [50, 51]. The variation of temperature from 300 to 1000 K for NVT ensemble and from 300 to 1200 K for NPT hoover ensemble was explored for the three h-BNNSs. In the process, the entropy and coefficient of linear thermal expansion were calculated. To achieve the objectives, the total energy of each supercell was plotted with respect to the changing temperature as displayed in Figure 4. To quantify the behaviour of 2D h-BNNSs energy against temperature, Figure 5 presents the suggested visual effects on these nanosheets at 1000 K for NVT and NPT ensembles for all the supercells. The structural stability of 2D h-BNNSs can also be demonstrated from the strain and stress point of view. It is known that there are only two energy components that contribute to the total energy for material to break under tensile loading, which are thermal and strain energy [52]. It has already been shown that the thermal energy of the materials for all the supercells increases linearly with temperature which implies that, the strain energy required for a material to break is reduced, due to the known inverse proportionality relationship between strain and thermal energy. As such, the stress will also reduce because of direct proportionality relationship between stress and strain. Therefore, the materials experience less strain and stress as the temperature gets intensified.

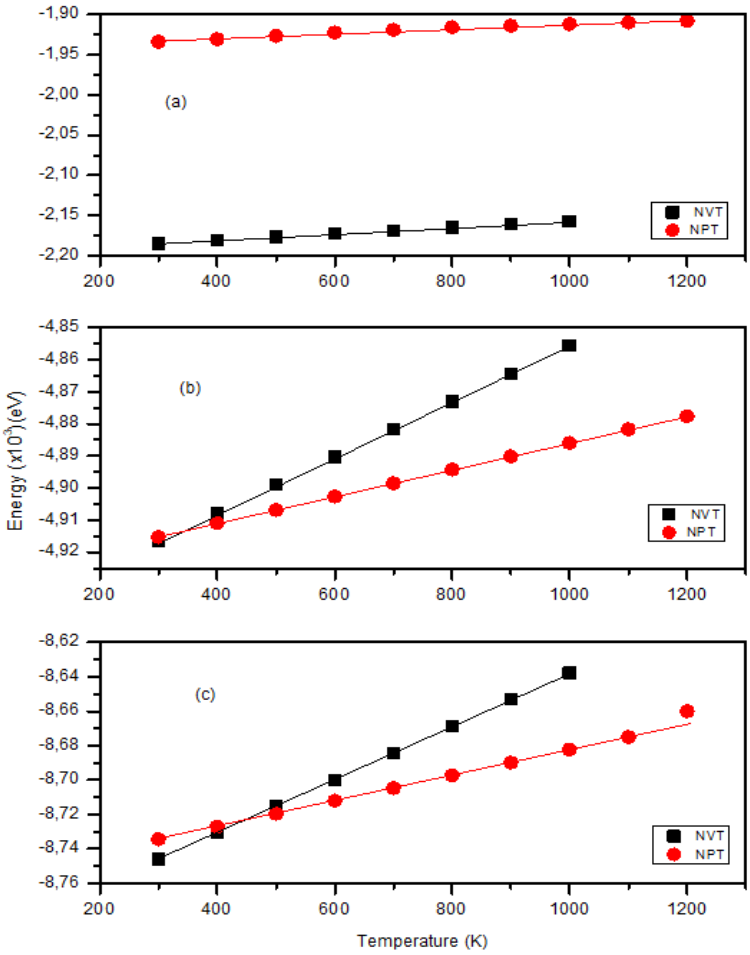

Figure 4: Graphs of total energy vs temperature for NVT and NPT ensembles of (a) h-BNNS144 (b) h-BNNS324 and (c) h-BNNS576 supercells.

The entropy change (ΔS) was then calculated using equation 2 for all the three supercells, as it is known in physics that, the unfound information about the state of a system can be related to the change in entropy of the system [53, 54]. The change in entropy in the supercells considered increases with an increase in the surface area of the materials, which actively demonstrates that, the number of possible arrangements of the atoms within the surface increases. This also contribute in the further understanding of the actual planar nanosheet geometry.

$$F=Eo\text{-}T\Delta S \quad (2)$$

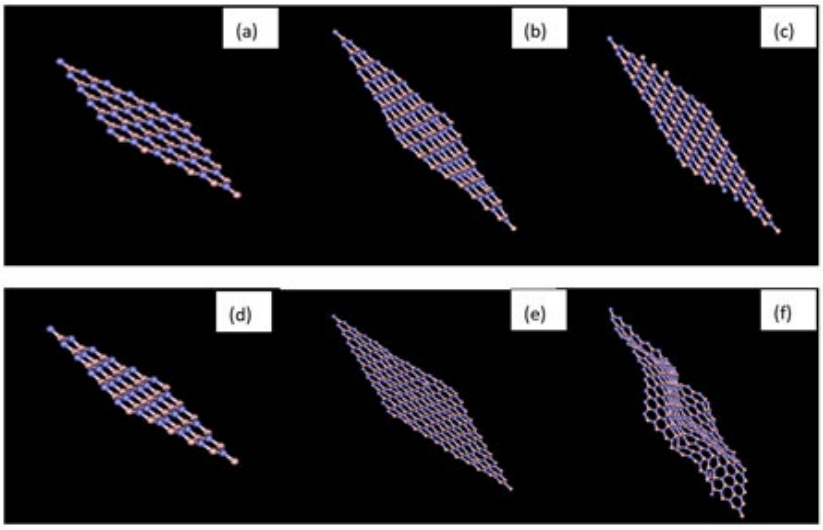

Figure 5: The visualisation of defect-free supercells structures represented by alternating B (brown spheres) and N (blue spheres) atoms for (a) h-BNNS144 NVT, (b) h-BNNS324 NVT, (c) h-BNNS576 NVT, (d) h-BNNS144 NPT, (e) h-BNNS324 NPT and (f) h-BNNS576 NPT ensembles at 1000 K.

In nanotechnology, materials that have both positive and negative thermal expansion coefficient are of practical importance as they can be utilized to make composites with very little thermal expansion/contraction [39]. In general, if a is the equilibrium lattice parameter and T is the corresponding temperature, then the linear thermal expansion coefficient $(a_l(T))$ can be calculated using equation 3:

$$a_l(T) = \frac{1}{a(T)}\left(\frac{\partial a(T)}{\partial T}\right)_p \qquad (3)$$

Thomas et al. [39] have disclosed that h-BN has a negative thermal expansion at low temperatures due to the low frequency bending modes in its phonon spectrum. Sevik et al. [40] also reported negative thermal expansion of h-BN below 300 K using a quasi-harmonic approximation (QHA) which gradually increases in the temperature range of 300 – 1500 K. Table 5 shows the values for the entropy change and linear thermal expansion coefficients. Figure 6 further presents the calculated coefficients of linear thermal expansions. It must be emphasized that on the linear thermal expansion coefficients of h-BNNS324 and h-BNNS576 the highlight is that the a-axis against temperature was separated into two sections: 300 – 500 K and 600 – 1000 K on h-BNNS324 and similarly 300 – 500 K and 600 – 1200 K.

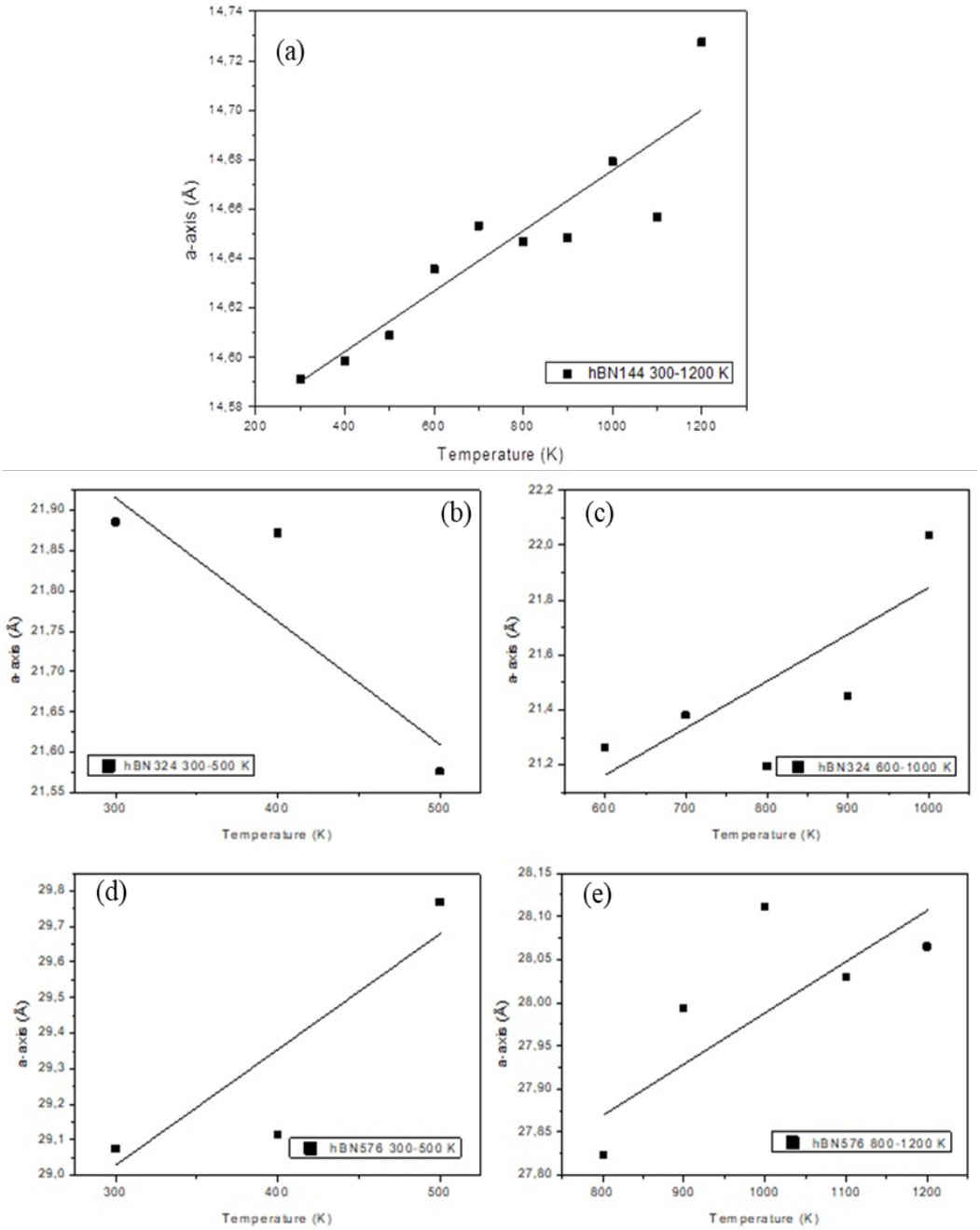

Figure 6: Graph of a-axis vs temperature for (a) h-BNNS144 from 300 – 1200 K temperature range, (b) h-BNNS324 from 300 – 500 K, (c) h-BNNS324 from 600 – 1000 K, (d) h-BNNS576 from 300 – 500 K and (e) h-BNNS576 from 800 – 1200 K for determining the coefficient of thermal expansion under NPT hoover ensemble.

Table 5: Calculated entropy change (ΔS) and coefficient of linear thermal expansion coefficient (a_l (*T*)) for the three studied supercells.

Supercells	Entropy change (eV/K)	Thermal expansion coefficient (K^{-1})
h-BNNS144	3.8×10^{-2}	1.50×10^{-3}
h-BNNS324	8.6×10^{-2}	-3.50×10^{-2} and3.50×10^{-2}
h-BNNS576	1.56×10^{-1}	1.02×10^{-1} and 1.45×10^{-2}

The results acquired using the NPT hoover ensemble shows that 2D h-BNNSs possesses a positive a_l of 1.50×10^{-3} K^{-1} for h-BNNS144 within the specified temperature range. The h-BNNS324 supercell possesses a negative a_l of -3.50×10^{-2} K^{-1} within a temperature range of 300 – 500 K and a positive a_l of 3.50×10^{-2} K^{-1} within a temperature range of 600 – 1000 K. In the case of h-BNNS576, two positive thermal expansion coefficients were observed; a_l of 1.02×10^{-1} K^{-1} in the temperature range of 300 – 500 K and a_l of 1.45×10^{-2} K^{-1} in the temperature range of 800 – 1200 K (see Table 5 for full results). Our study shows both positive and negative linear thermal expansion coefficients, which are comparable to the earlier studies, reported by Thomas *et al*. [39] for negative and Sevik *et al.* [40] within a range of 300 – 1500 K for positive thermal expansions. Thus, buckling of planes with elevated temperature is observed at 1200 K as shown in Figure 4(c) h-BN576 supercell NPT hoover ensemble.

3.3 Native defects in h-BNNSs

The computational analysis of defects for the calculations of mechanical properties promotes the understanding of the materials behaviour at various physical situations [39]. The effect of the defects in a 2D mono-layer system may be far more evident when compared with the bulk counterparts. This is because all atoms in a mono-layer nanosheet are in the surface on both sides of the plane. Therefore, the defects can change the properties of the material dramatically, due to the perturbation of the surface atomic arrangements [55]. Vacancies are the usual intrinsic defects in a 2D h-BN layer that needs special attention. The focus here is on the mono-vacancy defects, which are created by the removal of either B or N atom in h-BNNSs. The vacancies are randomly created in the h-BN nanosheet, were the variation of total energy with temperature generally demonstrate the structural changes. In all the three supercells, the B and N atomic vacancies were introduced with varying temperature from 300 – 1200 K in the NVT Evans ensemble. The energy versus temperature graphs of the entire setting is displayed in Figure 7. The interatomic potential model used in the present MD simulations are good in interpreting point defects [8].

In this setup, the B atom vacancy is represented by V_B and the N atom vacancy is represented by $V_{N.}$ The V_B and V_N defects on h-BNNS are constantly compared with the defect-free h-BN nanosheet. The energy-temperature graphs of both V_B and V_N for all the supercells in Figure 7, clearly shows the linearity and the proportionality relationship between energy and temperature. From these linear plots, calculation of the energy to create the vacancy (vacancy energy – E_{vac}) can be obtained using equation 4:

$$E_{vac} = E_{defect\text{-}free} - E_{defected} \quad (4)$$

where $E_{defect\text{-}free}$ and $E_{defected}$ represents the total energies of the defect-free and defected nanosheets for all the supercells. Furthermore, if $E_{defect\text{-}free}$ is the total energy of a system with N atoms, then the cohesive energy per particle can be expressed according to equation 5:

$$E_{coh} = \frac{E_{defect\ free}}{N} \quad (5)$$

where the cohesive energy of defect-free supercells was calculated to be E_{coh}= -15.2 *eV/atom* for all the three defect-free h-BNNSs supercells, which clearly shows a great mechanical strengths of the nanosheets with an increase in surface area respectively. Furthermore, the evaluation of vacancy energies of the defected nanosheets is simply the difference between the defect-free and that of defected nanosheet. According to the present study the V_B and V_N for h-BNNS143, h-BNNS323 and h-BNNS575 per defect are presented in Table 7. The tremendous difference on the values in relation to those in literature [37] might be due to various methodological procedures used in the modelling of the defects.

It could be noticed that the V_B and V_N have different E_{vac} in all the supercells, which clearly describes their state of stability as shown in Table 6. Moreover, the calculations show that the V_N has the lowest E_{vac} value as compared to V_B, which describes V_N as more stable than V_B, suggesting it to occur easily compared to V_B. Figure 8 displays the structural visualisation of V_B and V_N type defects at 300 K, which shows the random appearance of the position of a vacancy on surface of the material with an increase in surface area. These results were found to compare and concur well with the defect-free counterpart.

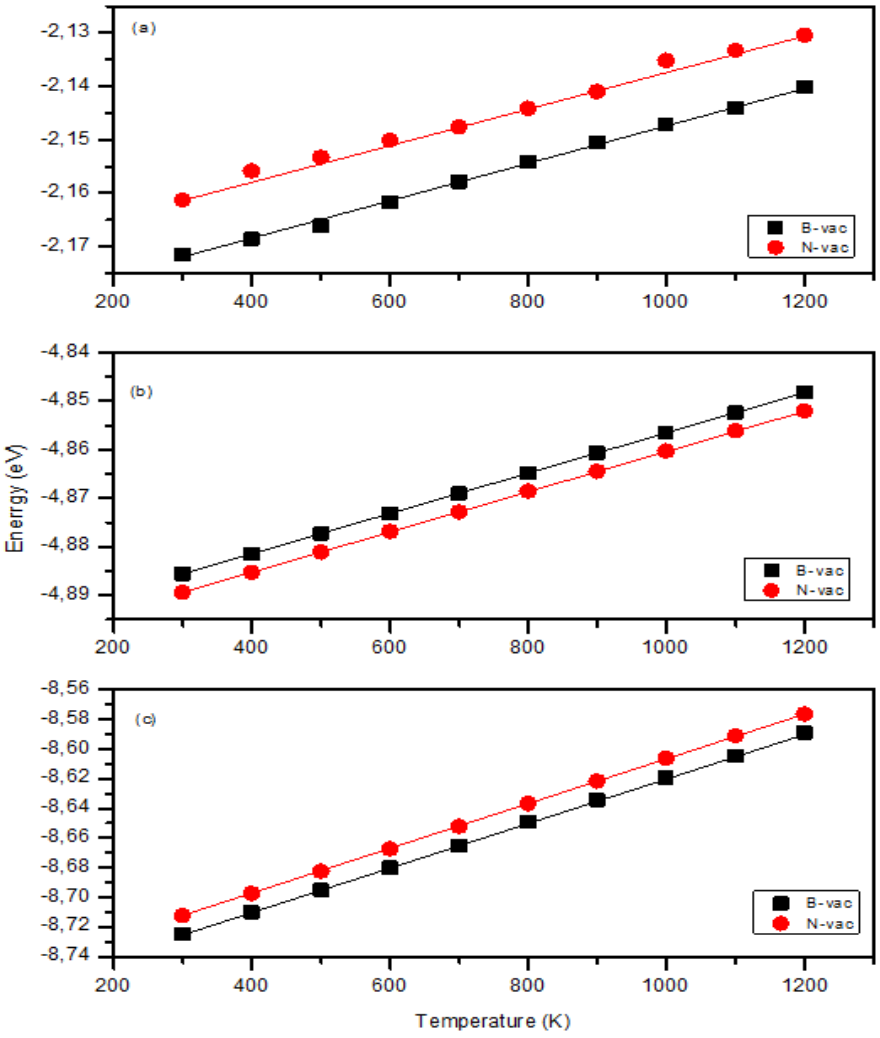

Figure 7: Graphs of energy as a function of temperature of V_B and V_N for (a) h-BNNS143 (b) h-BNNS323 and (c) h-BNNS575 NVT Evans ensemble.

Table 6: Minimum energy of defected h-BNNSs system, vacancy energy, volume and entropy change of a system of V_B, V_N and defect-free for h-BNNS143, h-BNNS323 and h-BNNS575 supercells at 300 K.

Supercells		V_B	V_N	Defect-free
h-BNNS143	Total energy (eV)	-2.1716×10^{3}	-2.1613×10^{3}	-2.1886×10^{3}
	Vacancy energy (eV)	-17	-27.3	-
	Volume (Å^3)	1.4969×10^{3}	1.4969×10^{3}	1.4969×10^{3}
	Entropy change (eV. K^{-1})	3.8×10^{-2}	3.0×10^{-2}	3.8×10^{-2}
h-BNNS323	Total energy (eV)	-4.9013×10^{3}	-4.8875×10^{3}	-4.9155×10^{3}
	Vacancy energy (eV)	-14.2	-28	-
	Volume (Å^3)	3.4796×10^{3}	3.4796×10^{3}	3.4796×10^{3}
	Entropy change (eV. K^{-1})	1.43×10^{-2}	1.43×10^{-2}	8.6×10^{-2}
h-BNNS575	Total energy (eV)	-8.7249×10^{3}	-8.7124×10^{3}	-8.7414×10^{3}
	Vacancy energy (eV)	-16.5	-29.0	-
	Volume (Å^3)	6.1461×10^{3}	6.1461×10^{3}	6.1461×10^{3}
	Entropy change (eV. K^{-1})	1.55×10^{-1}	1.53×10^{-1}	1.56×10^{-1}

Table 7: Calculated V_B and V_N defects energies for h-BNNS143, h-BNNS323 and h-BNNS575 per defect.

Supercells	V_B (eV)	V_N (eV)
h-BNNS143	-17.0	-27.3
h-BNNS323	-14.0	-28.0
h-BNNS575	-16.5	-29.0
Literature [37]	11.7	11.7

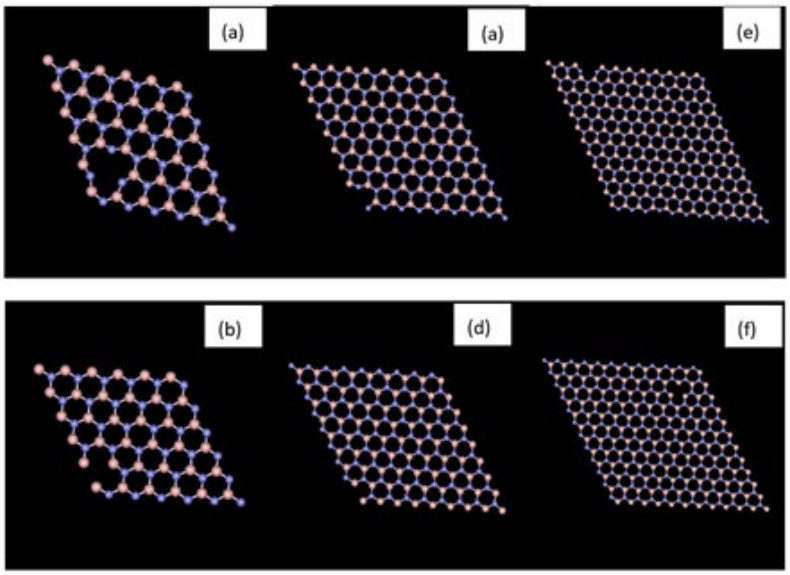

Figure 8: The visualisations of V_B and V_N represented by alternating B (brown spheres) and N (blue spheres) atoms respectively. (a) V_B for h-BNNS143, (b) V_N for h-BNNS143, (c) V_B for h-BNNS323, (d) V_N for h-BNNS323, (e) V_B for h-BNNS575 and (f) V_N for h-BNNS575 supercells.

4. Conclusion

The structural behaviour of defect-free, B and N vacancies in mono-layer 2D h-BNNSs atomic supercells have been studied with help of Tersoff potentials at different temperatures. The calculated $(g_{AB}(r))$ and $S(k)$ results demonstrated the consistency of Tersoff potentials in explaining the interaction between B and N atoms within the BN system, together with how B-B, B-N, and N-N bonds arrange and distribute themselves around a given atom. Of important highlight, introduction of V_B and V_N native defects does not necessarily affect the structural properties of the h-BN nanosheets. The calculated diffusion coefficients of B atoms were found to be increasing with an increase in the surface area. The entropy change, which was as well found to be increasing with surface area, provides explanation of the buckling of 2D planar layers at elevated temperatures. Such properties may as well be considered when exploring the semiconductor behaviour of the nanosheets. The coefficients of thermal expansions through the h-BNNSs demonstrate complex behaviour as the supercell surface area increases. This also further gives an explanation on the buckling and stiffling suggested for h-BNNSs. At larger surface areas, more coefficients of thermal expansion, which include both positive and negative values, are experienced. This idea is associated with the nanosheets bending and wrinkling as suggested by the experiments. V_N point defect was found to be more stable in all the studied formations and can easily occur than the V_B point defect. Introduction of these point defects may be useful when manipulating the h-BN nanosheets for semiconductor behaviour.

Author Contributions

Magopa T.M Kekana - Investigation, Methodology, Formal Analysis, Data curation, and writing – original draft
Thuto E. Mosuang – Conceptualization, Project administration, Resources, Software, Supervision, Writing – review & editing;
Nikiwe Mhlanga – Data curation, Formal analysis, Validation, writing – review & editing
Mokete A. Mahladisa – Data curation, Formal analysis, Methodology, validation, Writing – review & editing
Lucky M. Sikhwivhilu – Conceptualisation, Funding acquisition, Project administration, Resources, Supervision, Writing – review & editing.

Funding

Mintek, Department of Science and Innovation (DSI) - South Africa, through the DSI/Mintek Nanotechnology Innovation Centre (NIC), supported this work. The authors also acknowledge the University of Limpopo (UL) and University of Venda (UNIVEN) for the support. Furthermore, the authors wish to acknowledge the National Intellectual Property Management Office (NIPMO)-South Africa and the Centre for High-Performance Computing (CHPC).

Data Availability Statement

The data displayed in this work is available on request from the corresponding author.

Acknowledgments

The authors acknowledge Mintek, Centre for High Performance Computing (CHPC) and the University of Limpopo (UL) for financial support and research facilities.

Conflicts of Interest

The authors declare that there is no conflict of interest.

References

1. Thomas, S., Ajith, K. M., & Valsakumar, M. C. (2017). Empirical potential influence and effect of temperature on the mechanical properties of pristine and defective hexagonal boron nitride. Materials Research Express, 4(6), 065005.
2. Verma, V., Jindal, V. K., & Dharamvir, K. (2007). Elastic moduli of a boron nitride nanotube. Nanotechnology, 18(43), 435711.https://iopscience.iop.org/article/10.1088/0957-4484/18/43/435711/meta
3. Liao, L., Lin, Y. C., Bao, M., Cheng, R., Bai, J., Liu, Y., ... & Duan, X. (2010). High-speed graphene transistors with a self-aligned nanowire gate. Nature, 467(7313), 305-308.
4. Srivastava, P., & Sen, P. (2012). Density functional study of structural defects in h-BNC2 sheets. Journal of Physics: Condensed Matter, 25(2), 025304.
5. Devanathan, R., Krack, M. and Bertolus, M. (2015). Classical molecular dynamics simulation of nuclear fuels (No. NEA-NSC-R--2015-5).
6. Mermin, N. D. (1968). Crystalline order in two dimensions. Physical Review, 176(1), 250.
7. Kresse, G. (2002). Ab initio molecular dynamics: recent progresses and limitations. Journal of non-crystalline solids, 312, 52-59.
8. Matsunaga, K., Fisher, C., & Matsubara, H. (2000). Tersoff potential parameters for simulating cubic boron carbonitrides. Japanese Journal of Applied Physics, 39(1A), L48.
9. Lipp, A., Schwetz, K. A., & Hunold, K. (1989). Hexagonal boron nitride: fabrication, properties and applications. Journal of the European Ceramic Society, 5(1), 3-9.
10. Meric, I., Dean, C. R., Petrone, N., Wang, L., Hone, J., Kim, P., & Shepard, K. L. (2013). Graphene field-effect transistors based on boron–nitride dielectrics. Proceedings of the IEEE, 101(7), 1609-1619.
11. Chen, Y., Zou, J., Campbell, S. J., & Le Caer, G. (2004). Boron nitride nanotubes: Pronounced resistance to oxidation. Applied physics letters, 84(13), 2430-2432.
12. Ma, R.; Bando, Y.; Sato, T.; Kurashima, K. Growth, Morphology, and Structure of Boron Nitride Nanotubes. Chemistry of Materials 2001, 13, 2965-2971.
13. Kim, K. K., Hsu, A., Jia, X., Kim, S. M., Shi, Y., Dresselhaus, M., ... & Kong, J. (2012). Synthesis and characterization of hexagonal boron nitride film as a dielectric layer for graphene devices. ACS nano, 6(10), 8583-8590.
14. Youngblood, N., & Li, M. (2017). Integration of 2D materials on a silicon photonics platform for optoelectronics applications. Nanophotonics, 6(6), 1205-1218.
15. Britnell, L., Gorbachev, R. V., Jalil, R., Belle, B. D., Schedin, F., Katsnelson, M. I., ... & Novoselov, K. S. (2012). Electron tunneling through ultrathin boron nitride crystalline barriers. Nano letters, 12(3), 1707-1710.
16. Liu, N., & Gao, Y. (2017). Recent progress in micro-supercapacitors with in-plane interdigital electrode architecture. Small, 13(45), 1701989.
17. Esrafili, M. D., & Saeidi, N. (2017). N2O+ SO2 reaction over Si-and C-doped boron nitride nanotubes: A comparative DFT study. Applied Surface Science, 403, 43-50.
18. Fandrich, M., Mehrtens, T., Aschenbrenner, T., Klein, T., Gebbe, M., Figge, S., ... & Hommel, D. (2013). Nitride based heterostructures with Ga-and N-polarity for sensing applications. Journal of crystal growth, 370, 68-73.
19. Yu, S., Wang, X., Pang, H., Zhang, R., Song, W., Fu, D., ... & Wang, X. (2018). Boron nitride-based materials for the removal of pollutants from aqueous solutions: a review. Chemical Engineering Journal, 333, 343-360.
20. Lee, C., Wei, X., Kysar, J. W., & Hone, J. (2008). Measurement of the elastic properties and intrinsic strength of monolayer graphene. science, 321(5887), 385-388.
21. Cui, T., Mukherjee, S., Sudeep, P. M., Colas, G., Najafi, F., Tam, J., ... & Filleter, T. (2020). Fatigue of graphene. Nature materials, 19(4), 405-411.
22. Cui, G., Bi, Z., Zhang, R., Liu, J., Yu, X., & Li, Z. (2019). A comprehensive review on graphene-based anti-corrosive coatings. Chemical Engineering Journal, 373, 104-121.
23. Tersoff, J. (1988). New empirical approach for the structure and energy of covalent systems. Physical review B, 37(12), 6991.
24. Tersoff, J. (1988). Empirical interatomic potential for carbon, with applications to amorphous carbon. Physical Review Letters, 61(25), 2879.
25. Erhart, P., & Albe, K. (2005). Analytical potential for atomistic simulations of silicon, carbon, and silicon carbide. Physical Review B, 71(3), 035211.
26. Lindsay, L., & Broido, D. A. (2010). Optimized Tersoff and Brenner empirical potential parameters for lattice dynamics and phonon thermal transport in carbon nanotubes and graphene. Physical Review B, 81(20), 205441.
27. Agrawal, P. M., Raff, L. M., & Komanduri, R. (2005). Monte Carlo simulations of void-nucleated melting of silicon via modification in the Tersoff potential parameters. Physical Review B, 72(12), 125206.
28. Smith, R. (1992). A semi-empirical many-body interatomic potential for modelling dynamical processes in gallium arsenide. Nuclear Instruments and Methods in Physics Research Section B: Beam Interactions with Materials and Atoms, 67(1-4), 335-339.
29. Sayed, M., Jefferson, J. H., Walker, A. B., & Cullis, A. G. (1995). Molecular dynamics simulations of implantation damage and recovery in semiconductors. Nuclear Instruments and Methods in Physics Research Section B: Beam Interactions with Materials and Atoms, 102(1-4), 218-222.
30. Nordlund, K., Nord, J., Frantz, J., & Keinonen, J. (2000). Strain-induced Kirkendall mixing at semiconductor interfaces. Computational materials science, 18(3-4), 283-294.
31. Powell, D., Migliorato, M. A., & Cullis, A. G. (2007). Optimized Tersoff potential parameters for tetrahedrally bonded III-V semiconductors. Physical Review B, 75(11), 115202.
32. Moon, W. H., & Hwang, H. J. (2003). Structural and thermodynamic properties of GaN: a molecular dynamics simulation. Physics Letters A, 315(3-4), 319-324.
33. Goumri-Said, S., Kanoun, M. B., Merad, A. E., Merad, G.,

& Aourag, H. (2004). Prediction of structural and thermodynamic properties of zinc-blende AlN: molecular dynamics simulation. Chemical Physics, 302(1-3), 135-141.
34. Sevik, C., Kinaci, A., Haskins, J. B., & Çağın, T. (2011). Characterization of thermal transport in low-dimensional boron nitride nanostructures. Physical Review B, 84(8), 085409.
35. Mortazavi, B., Cuniberti, G., & Rabczuk, T. (2015). Mechanical properties and thermal conductivity of graphitic carbon nitride: A molecular dynamics study. Computational Materials Science, 99, 285-289.
36. Srivastava, P., & Sen, P. (2012). Density functional study of structural defects in h-BNC2 sheets. Journal of Physics: Condensed Matter, 25(2), 025304.
37. Slotman, G. J., & Fasolino, A. (2012). Structure, stability and defects of single layer hexagonal BN in comparison to graphene. Journal of Physics: Condensed Matter, 25(4), 045009.
38. Paszkowicz, W., Pelka, J. B., Knapp, M., Szyszko, T., & Podsiadlo, S. J. A. P. A. (2002). Lattice parameters and anisotropic thermal expansion of hexagonal boron nitride in the 10–297.5 K temperature range. Applied Physics A, 75(3), 431-435.
39. Thomas, S., Ajith, K. M., Chandra, S., & Valsakumar, M. C. (2015). Temperature dependent structural properties and bending rigidity of pristine and defective hexagonal boron nitride. Journal of Physics: Condensed Matter, 27(31), 315302.
40. Sevik, C. (2014). Assessment on lattice thermal properties of two-dimensional honeycomb structures: Graphene, h-BN, h-MoS 2, and h-MoSe 2. Physical Review B, 89(3), 035422.
41. Yuan, J., & Liew, K. M. (2014). Structure stability and high-temperature distortion resistance of trilayer complexes formed from graphenes and boron nitride nanosheets. Physical Chemistry Chemical Physics, 16(1), 88-94.
42. Barnard, A. S., Snook, I. K., & Russo, S. P. (2007). Bonding and structure in B x N y nanotubes (x, y= 1, 2). Journal of Materials Chemistry, 17(28), 2892-2898.
43. Liu, Y., Bhowmick, S., & Yakobson, B. I. (2011). BN white graphene with "colorful" edges: The energies and morphology. Nano letters, 11(8), 3113-3116.
44. Liu, Z. Q., Dong, J., & Ding, F. (2019). The geometry of hexagonal boron nitride clusters in the initial stages of chemical vapor deposition growth on a Cu (111) surface. Nanoscale, 11(28), 13366-13376.
45. Huang, B., Lee, H., Gu, B. L., Liu, F., & Duan, W. (2012). Edge stability of boron nitride nanoribbons and its application in designing hybrid BNC structures. Nano Research, 5(1), 62-72.
46. Zhang, Z., Liu, Y., Yang, Y., & Yakobson, B. I. (2016). Growth mechanism and morphology of hexagonal boron nitride. Nano letters, 16(2), 1398-1403.
47. Tay, R. Y., Griep, M. H., Mallick, G., Tsang, S. H., Singh, R. S., Tumlin, T., ... & Karna, S. P. (2014). Growth of large single-crystalline two-dimensional boron nitride hexagons on electropolished copper. Nano letters, 14(2), 839-846.
48. Albe, K., Möller, W., & Heinig, K. H. (1997). Computer simulation and boron nitride. Radiation Effects and Defects in Solids, 141(1-4), 85-97.
49. Alem, N., Erni, R., Kisielowski, C., Rossell, M. D., Gannett, W., & Zettl, A. J. P. R. B. (2009). Atomically thin hexagonal boron nitride probed by ultrahigh-resolution transmission electron microscopy. Physical Review B, 80(15), 155425.
50. Huang, J. Y., Chen, S., Wang, Z. Q., Kempa, K., Wang, Y. M., Jo, S. H., ... & Ren, Z. F. (2006). Superplastic carbon nanotubes. Nature, 439(7074), 281-281.
51. Tang, C., Guo, W., & Chen, C. (2009). Molecular dynamics simulation of tensile elongation of carbon nanotubes: temperature and size effects. Physical Review B, 79(15), 155436.
52. Zhang, Y. Y., & Gu, Y. (2013). Mechanical properties of graphene: Effects of layer number, temperature and isotope. Computational Materials Science, 71, 197-200.
53. Hopfield, J. J., & Herz, A. V. (1995). Rapid local synchronization of action potentials: toward computation with coupled integrate-and-fire neurons. Proceedings of the National Academy of Sciences, 92(15), 6655-6662.
54. Khordad, R., & Sedehi, H. R. (2017). Application of different entropies to study of bound magnetopolaron in an asymmetric quantum dot. Indian Journal of Physics, 91(7), 825-831.
55. Ribeiro, R. M., & Peres, N. M. R. (2011). Stability of boron nitride bilayers: Ground-state energies, interlayer distances, and tight-binding description. Physical Review B, 83(23), 235312.